OpenSky: a modular and open-source simulator of sky polarization measurements

Antoine Moutenet, Léo Poughon, Bruno Toulon, Julien R. Serres, Stéphane Viollet

***Abstract*—Autonomous navigation requires robust strategies, particularly in GPS-denied environments. Of great interest for geolocation or to estimate North is the measurement and processing of polarized skylight patterns. In this study, we fully describe an open source and easily upgradable simulator, named OpenSky, which can simulate the measurement of sky polarization properties, i.e., the light intensity, the angle of polarization and the degree of linear polarization of light seen through a polarimetric camera. OpenSky is an open source simulator available on open repositories (Github and Open Science Framework). It structured around 5 blocks, each of which can easily be improved, replaced or completed by users. These blocks individually simulate sky polarization properties, skylight intensity, optical conjugation, polarizing filters and sensors. The high fidelity of OpenSky was assessed by comparing the simulated camera captures to experimental raw images, from which both the angle and the degree of polarization were extracted by image processing. OpenSky will be useful for developing novel celestial-based sensors and estimating their potential relevance to scientific communities (fundamental or applied sciences). OpenSky could also become a powerful tool to train or validate deep neural networks. One major interest is the ability of the OpenSky simulator to generate many sky conditions at various positions on Earth, which can be difficult and costly to obtain in real world.**

***Index Terms*—celestial compass, skylight polarization, polarized camera, polarized vision, pattern of polarization, biomimetics, biomimetism, sky simulation, multiphysics modeling.**

I. INTRODUCTION

SUNLIGHT is unpolarized in space but it changes once it enters the atmosphere. When light is scattered by the molecules of the atmosphere, its properties change leading to the alterations in sky color, from blue during day to red at sunset, and it gains specific polarization properties. Numerous animals, especially insects like bees [1], ants [2], dung beetles [3], locusts [4], monarch butterflies [5] and flies [6], [7] are able to process skylight polarization for navigational purposes, in the visible spectrum but also into the UV band [8]. This property provides these animals with a remarkable advantage for short or long-range navigation. Humans are not sensitive to light polarization but polarimetric cameras have are used to augment the sensing repertoire. These cameras already led to the realization of a commercial optical compass based on skylight polarization [9] and are also considered to be of great interest for autonomous driving vehicles [10]–[12] , allowing systems to more easily measure and integrate the car's direction, especially in GNSS denied environments. Among the studies on bio-inspired polarized skylight navigation [13], many involve the use of polarimetric cameras equipped with fisheye objectives and pointed toward the sky in order to locate North [14]–[16] or even to implement geolocation [17]–[27]. However, none of the skylight polarization pattern simulations among those studies has proposed a complete model of sky polarization measurement, with a simulated sky coupled with a simulated camera. This is what our study describes. Since the whole measurement channel should be involved in the generation of measured skylight polarization patterns, we propose a way to implement it.

In this study, we first rely on the Rayleigh scattering model to provide a description of the polarization properties of atmospheric scattering and to define the local and global angles of polarization, which could be a source of confusion. Then, we switch to the Berry model that accounts for multiple scattering and the four neutral points observed in the polarization pattern [28]. Working with the Berry model, we propose a new rigorous computation of the degree of linear polarization relying on, as does the original model, the Brewster definition of the intensity of polarization [29], which seems to be commonly mistaken for the degree of polarization.

Our simulator, named OpenSky, provides a full simulation from atmosphere scattering to the pixel output signal of a polarimetric camera. Within OpenSky, we have integrated a relative sky radiance computation based on the CIE luminance model [30]–[34], and an optical conjugation model including thin lens and various fisheye objectives that can be mounted onto the camera [35]. Finally, we implemented a model of a full imager polarimetric sensor, which is composed of several square blocks of 4 linearly polarized pixels [36]. The transmitted light through the micro-polarizer array was computed as classically in the literature [37] and the output signal of each pixel was computed regarding sensor dynamic range, electrical noise and light saturation.

In previous studies of open-source polarized skylight simulators, there was a notable absence: these programs lacked a model simulating a camera at the pixel level [38]–[40] or a module that accounts for the large changes in the sky irradiance [39]. The goal of our work was to implement a fully open source and easily modifiable program which can faithfully simulate the measurement of sky polarization properties, which means simulating polarized skylight

---

This work was supported by CNRS and Aix-Marseille University. A.M. was supported by a CIFRE doctoral fellowship from the ANRT and Safran Electronics & Defense (agreement #2021/0056). J.R.S has received funding from the Excellence Initiative of Aix-Marseille Université - A*Midex, a French "Investissements d'Avenir" programme AMX-21-ERC-02 and AMX-20-TRA-043. This research work was also supported by the SUD Provence-Alpes-Côte d'Azur Region (PACA) (Grant #2021/08135). The authors would like to thank David Wood (English at your Service, http://www.eays.eu/, accessed on 30 August 2023) the English of the manuscript.

patterns, sensor devices and image processing. To achieve these successive stages, we chose to build a program divided into 5 modular blocks (6 if we include image processing), each one can easily be improved, replaced or customised by users. In order to validate our complete simulator, we compared digital simulations of our sensors under clear and more or less cloudy skies against experimental outdoor measurements. OpenSky can be considered as a new tool to rigorously simulate polarized skylight patterns measured by a polarimetric camera, composed of a 2D array of linear polarizers. It could offer new perspectives for biologists to simulate visual perception and processing stages in animals behavior modeling [41], [42]. It could also open a new avenue toward the generation of image data composed of polarimetric images for the training and the validation of neural networks [18], [43]–[45] or the validation of new polarization-based underwater geolocalization equipment. [24], [26].

Section II describes the polarization formalism. Sections III and IV thoroughly depict thoroughly the Rayleigh model and how our local and global angles of polarization are defined. Section V explains our implementation of the Berry model. Section VI revisits the CIE model of sky radiance and explains how we used it. Section VII describes our optical conjugation model. Section VIII describes our models for the micropolarizer array and pixel output. Section IX describes the simulator structure. Finally, section X compares OpenSky simulation data with experimental data.

TABLE I

VARIABLES USED IN THIS STUDY

AoP	angle of polarization, which express the polarization vector direction in a particular frame
AoP_l	angle of polarization express in the incoming ray (local) frame
AoP_g	angle of polarization in observer frame
DoP	degree of polarization
$DoLP$	degree of linear polarization
$DoLP_{max}$	maximum degree of linear polarization in sky
γ	scattering angle
α_s , θ_s	sun azimuth and elevation
α_p , θ_p	random sky particle azimuth and elevation
φ_s	sun zenith angle
φ_p	random sky particle zenith angle
E_{inc} , I_{inc}	amplitude and (simplified) intensity of the incident electrical field
E_{scat} , I_{scat}	amplitude and (simplified) intensity of the scattered electrical field
$E_{\mathrm{x}_\perp}$, $I_{\mathrm{x}_\perp}$	amplitude and (simplified) intensity of the component of the X electrical field orthogonal to the scattering plan
$E_{\mathrm{x}_\parallel}$, $I_{\mathrm{x}_\parallel}$	amplitude and (simplified) intensity of the component of the X electrical field parallel to the scattering plan
$I_{\mathrm{x}_{pol}}$, $I_{\mathrm{x}_{unpol}}$	(simplified) intensity of the component of the X electrical field totally polarized, respectively totally unpolarized
IoP	intensity of polarization
$I_0, I_{45}, I_{90}, I_{135}$	light intensities linearly polarized at 0°, 45°, 90°, 135° in a given frame
$I_{\mathrm{C_R}}$, $I_{\mathrm{C_L}}$	light intensities circularly right and left polarized in a given frame
a , e	azimuth and ellipticity angles of polarization’s ellipse in Jones Formalism
S_0 , S_1 , S_2 , S_3	Stokes vector parameters
$\vec{s}$	polarization state vector in Poincaré sphere
s_x , s_y , s_z	x,y,z coordinate of the polarization state vector in Poincaré sphere
P	particle point, it is a point at unitary distance from the observer which gives a direction of observation in the atmosphere
x_{proj}	stereographic or orthogonal projection of X
$\overrightarrow{OP}$, $\overrightarrow{OS}$	observer-particle and observer-sun unit vectors
$\overrightarrow{E_{dir}}$	vector which carries direction of polarization
$\overrightarrow{x_{mer}}$, $\overrightarrow{y_{mer}}$, $\overrightarrow{z_{mer}}$	meridian direct frame
ξ_+	complex coordinates of stereographic projection of Brewster neutral point
ξ_-	complex coordinates of stereographic projection of Babinet neutral point
δ	positive angle between the neutral points Brewster and Babinet or Arago and the Fourth
$w()$	Berry complex function
$A, B, C, D, E_{\mathrm{CIE}}$	CIE’s standard sky coefficients
L_{rel}	relative sky luminance (always takes value 1 at the zenith)
θ	angle of an object point at infinite distance from the optic
f	focal length
r	positive distance between an image point and the optical axis
r_{x}	positive distance between an image point and the optical axis for the optical conjugation model number X
ψ	passing linear polarization angle of polarizers
ψ_{perfect} , $\Delta\psi$	passing linear polarization angle of polarizers perfectly set and passing linear polarization angle error
T_1 , T_2	polarizers’ transmittance for respectivly the passing and blocking axes
ε	polarization efficiency of polarizers
SNR	Signal-to-Noise-Ratio
R_{sat}	saturation ratio equal to max intensity coming to pixels’sensor and saturation intensity of pixels’ sensor
N_{bit}	number of bits per pixel of the sensor output
I_{in} , I_{out}	relative light intensity before and after passing through polarizers
$I_{out_{max}}$	maximum relative light intensity after polarizers
ΔG	random Gaussian noise
P_{output}	grayscale intensity returned by each pixel of the sensor

II. Polarization and Stokes formalism

We recall here the basic principles of polarization in order to define the parameters used in our simulator. Light is polarized when the electrical vector field at given point in space is moving elliptically over time. Usually the ellipse of polarization is described using two parameters: the great axis azimuth (a) and the ellipticity angle (e), which is the angle between the great axis and the diagonal of the smallest rectangle containing the ellipse, this angle is positive / negative when the electric field rotates counter-clockwise / clockwise around the propagation axis over time (Fig. 1a).

When ellipticity is null, polarization is linear, which is the case in atmospheric scattering polarization. Since the light can be partially polarized, a common term was created: the degree of polarization (DoP). The DoP is the ratio between polarized light intensity and total light intensity I_{total}. These three parameters, a, e and DoP, describe all partially polarized light and provide a geometric representation of the polarization state in a space called the Poincaré sphere. In the Poincaré sphere, a polarization state is a vector $\vec{s}$ of azimuth $2a$, elevation $2e$ and norm DoP (Fig. 1b). Another common way to describe polarized light is the Stokes formalism with the Stokes vector. Stokes vectors are vectors composed of four parameters (S_0, S_1, S_2, S_3) defined by (1) where I_0, I_{90}, I_{45}, I_{135}, I_{C_L} and I_{C_R} are the intensities of light respectively linearly polarized at 0°, 90°, 45° and 135° and circularly polarized in counter-clockwise sense and clockwise sense.

$$\left\{\begin{array}{l} S_0 \\ S_1 \\ S_2 \\ S_3 \end{array}\right. = \left\{\begin{array}{l} I_0 + I_{90} = I_{\text{total}} \\ I_0 - I_{90} \\ I_{45} - I_{135} \\ I_{\text{C}_\text{L}} - I_{\text{C}_\text{R}} \end{array}\right. \tag{1}$$

The Stokes formalism fits well with the Poincaré sphere since $\vec{s}$ could also be described as a normalized Stokes vector (2):

$$\vec{s} = (1/S_0) \cdot (S_1, S_2, S_3) \tag{2}$$

III. Skylight polarization and Rayleigh scattering

The most common way to describe atmospheric scattering near the visible spectrum is the Rayleigh model (1871), which describes all the electromagnetic field properties considering single elastic scattering by particles much smaller than the wavelength. Amongst all the parameters resulting from Rayleigh scattering, in our study, we focus only on polarization.

A simplified way to model atmospheric scattering properties is to consider a small charged particle vibrating according to the incident (coming from sun) electrical field perturbation. This particle itself will generate electrical field perturbations, according to its vibrating directions, which will be seen differently depending on the observer's position (Fig. 2).

We define the scattering plane as that formed by the directions of the incoming light and the scattered light, that means it contains the sun, the observed particle and the observer (Fig. 3b).

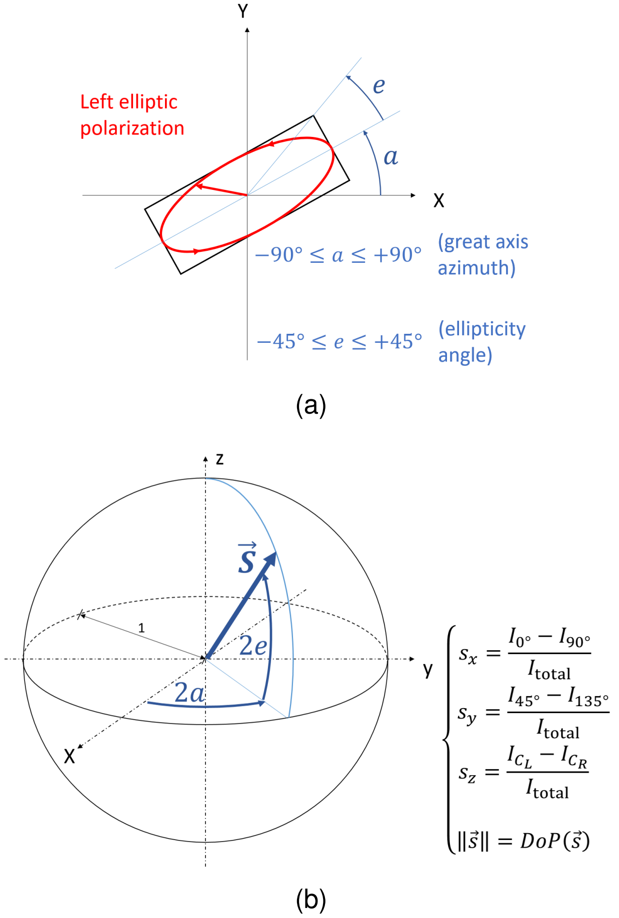

Fig. 1. Polarization formalism. (a) Polarization ellipse, where the z axis is the propagation axis (here it goes toward the reader). (b) Poincaré sphere and representation of polarization state

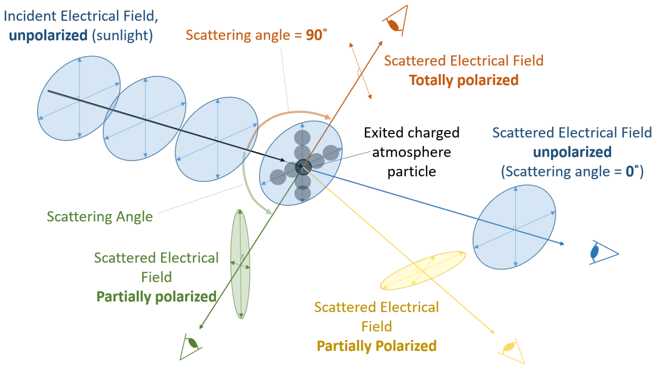

Fig. 2. Illustration of the polarization phenomenon for a small particle simple elastic scattering model.

All effects resulting from wavelength and absorption aside, if we consider the incident electrical field along two orthogonal axes, one parallel to and one perpendicular to the scattering plane, we can observe that perpendicular component is fully transmitted, and the parallel component is partially transmitted (Fig. 3a), according to a cosine law of the scattering angle γ (3).

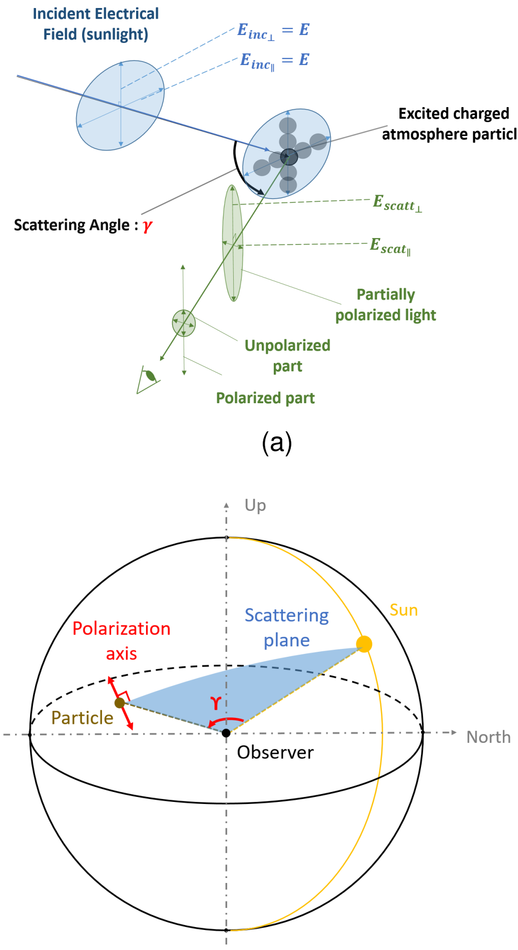

(a)

(b)

Fig. 3. Scattering plane and polarized components. (a) Polarization phenomenon for small particle simple elastic scattering model. (b) Description of the scattering plane.

$$\begin{cases} E_{scat_\perp} \propto E_{inc_\perp} = E \\ E_{scat_\parallel} \propto E_{inc_\parallel} \cdot \cos(\gamma) = E \cdot cos(\gamma) \end{cases} \tag{3}$$

Since it is common use to consider light intensity as the electrical field amplitude squared, we get the two scattered intensity components:

$$\begin{cases} I_{scat_\perp} = E^2 \\ I_{scat_\parallel} = E^2 \cdot \cos(\gamma)^2 \end{cases} \tag{4}$$

In order to find out the polarization properties, we need to consider the scattering light as the sum of a polarized component and a unpolarized component, which gives us the following intensities:

$$\begin{cases} I_{scat} = I_{scat_\perp} + I_{scat_\parallel} \\ I_{scat_{unpol}} = 2 \cdot I_{scat_\parallel} \\ I_{scat_{pol}} = I_{scat_\perp} - I_{scat_\parallel} \end{cases} \tag{5}$$

Those two intensity components, polarized ($I_{scat_{pol}}$) and unpolarized ($I_{scat_{unpol}}$), allow us to express the degree of linear polarization ($DoLP$):

$$DoLP = \frac{I_{scat_{pol}}}{I_{scat}} = \frac{E^2 - E^2 \cdot \cos(\gamma)^2}{E^2 + E^2 \cdot \cos(\gamma)^2} = \frac{\sin(\gamma)^2}{1+\cos(\gamma)^2} \tag{6}$$

We deal with $DoLP$ because the atmospheric elastic scattering only involves linear polarization. As written in (6), $DoLP$ takes values from 0 to 1 but in real conditions, i.e. atmospheric multiple scattering, the $DoLP$ never reaches 1. Knowing this $DoLP$ is usually corrected with a maximum value coefficient, $DoLP_{max}$, which is the maximum observable $DoLP$, depending on sky turbidity (usually 0.75 for a clear sky):

$$DoLP = \frac{sin(\gamma)^2}{1 + cos(\gamma)^2} \cdot DoLP_{max} \tag{7}$$

IV. POLARIZATION ANGLE, LOCAL FRAME AND OBSERVER FRAME

In this study, we use the coordinate system depicted in Fig. 4. We do not refer to the usual East-North-Up (ENU) coordinate setup but to an observer frame, which is defined by an observer reference direction and shares its Up axis with the ENU frame, in order to facilitate the simulation of the sensor response. Actually, as explained in Section VIII, we use the length axis of the sensor's CMOS or CCD matrix as observer reference direction.

As shown in Fig. 4, in the observer frame, the observed points are described on a unit sphere with two coordinates: the elevation and the azimuth, respectively θ_p and α_p for random particle coordinates and respectively θ_s and α_s for sun coordinates.

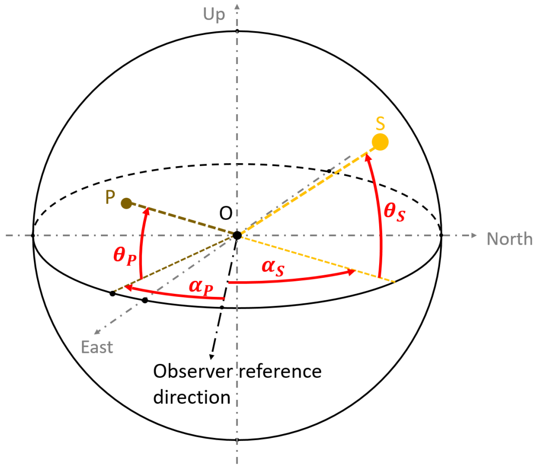

Fig. 4. Observed particle coordinates and sun coordinates in the observer frame. With the points O for the observer, P for the observed particle and S for the Sun

Since we know that the polarization axis is orthogonal to the scattering plane (Fig. 3b), we can characterize it in our observer frame with an orientation angle. This angle is usually called the angle of polarization (AoP) and ranges from 0 to 180°. The AoP distribution properties will change depending on the frame used to describe it [46].

In this study, we use two different AoP: the angle between the polarization axis and the particle meridian plane noted as AoP_l (Fig. 5a) and the angle between polarization axis and the observer reference direction (Fig. 5b) noted as AoP_g. The particle meridian plane is the plane which contains the observer, the zenith axis (true vertical) and the observation direction. The local angle of polarization AoP_l is associated with the direction light is coming from (same physical signification as a in Fig. 1a) while the global angle of polarization AoP_g, defined afterwards, is associated to our observer frame and will serve to characterize the polarization axis orientation, after optical conjugation, regarding the orientation of static polarizers set on the sensor.

To define the local angle of polarization AoP_l according to the Rayleigh model, we first define the associated meridian frame $P, \overrightarrow{x_{mer}}, \overrightarrow{y_{mer}}, \overrightarrow{z_{mer}}$ and the observer-sun vector:

$$
\begin{aligned}
\overrightarrow{z_{mer}} &= -\overrightarrow{OP} = \begin{cases} -\cos(\theta_p)\cdot\cos(\alpha_p) \\ -\cos(\theta_p)\cdot\sin(\alpha_p) \\ -\sin(\theta_p) \end{cases} ; \\
\overrightarrow{y_{mer}} &= \begin{cases} -\sin(\alpha_p) \\ \cos(\alpha_p) \\ 0 \end{cases} ; \\
\overrightarrow{x_{mer}} &= \overrightarrow{y_{mer}} \times \overrightarrow{z_{mer}} = \begin{cases} -\cos(\alpha_p)\cdot\sin(\theta_p) \\ -\sin(\alpha_p)\cdot\sin(\theta_p) \\ \cos(\theta_p) \end{cases} ; \\
\overrightarrow{OS} &= \begin{cases} \cos(\theta_s)\cdot\cos(\alpha_s) \\ \cos(\theta_s)\cdot\sin(\alpha_s) \\ \sin(\theta_s) \end{cases}
\end{aligned}
\tag{8}
$$

with $\overrightarrow{OP}$ and $\overrightarrow{OS}$ the observer-particle and observer-sun vectors. Then, we can express the axis of polarization through its direction vector $\overrightarrow{E_{dir}}$ this way:

$$
\begin{aligned}
&\overrightarrow{E_{dir}} = \overrightarrow{OP} \times \overrightarrow{OS} = \\
&\begin{cases} \cos(\theta_p)\cdot\sin(\alpha_p)\cdot\sin(\theta_s) - \sin(\theta_p)\cdot\cos(\theta_s)\cdot\sin(\alpha_s) \\ \sin(\theta_p)\cdot\cos(\theta_s)\cdot\cos(\alpha_s) - \cos(\theta_p)\cdot\cos(\alpha_p)\cdot\sin(\theta_s) \\ \cos(\theta_s)\cdot\cos(\theta_p)\cdot\sin(\alpha_s - \alpha_p) \end{cases}
\end{aligned}
\tag{9}
$$

Finally, since we have $\overrightarrow{E_{dir}}$, we can obtain the AoP_l, usually described by its tangent:

$$
\begin{aligned}
\tan(AoP_l) &= -\frac{\overrightarrow{E_{dir}}\cdot\overrightarrow{y_{mer}}}{\overrightarrow{E_{dir}}\cdot\overrightarrow{x_{mer}}} \\
&= \frac{\sin(\theta_p)\cdot\cos(\theta_s)\cdot\cos(\alpha_p-\alpha_s) - \cos(\theta_p)\cdot\sin(\theta_s)}{\cos(\theta_s)\cdot\sin(\alpha_p-\alpha_s)}
\end{aligned}
\tag{10}
$$

The AoP_g is defined through AoP_l, as shown in Fig. 5b:

$$AoP_g = AoP_l + \alpha_p \tag{11}$$

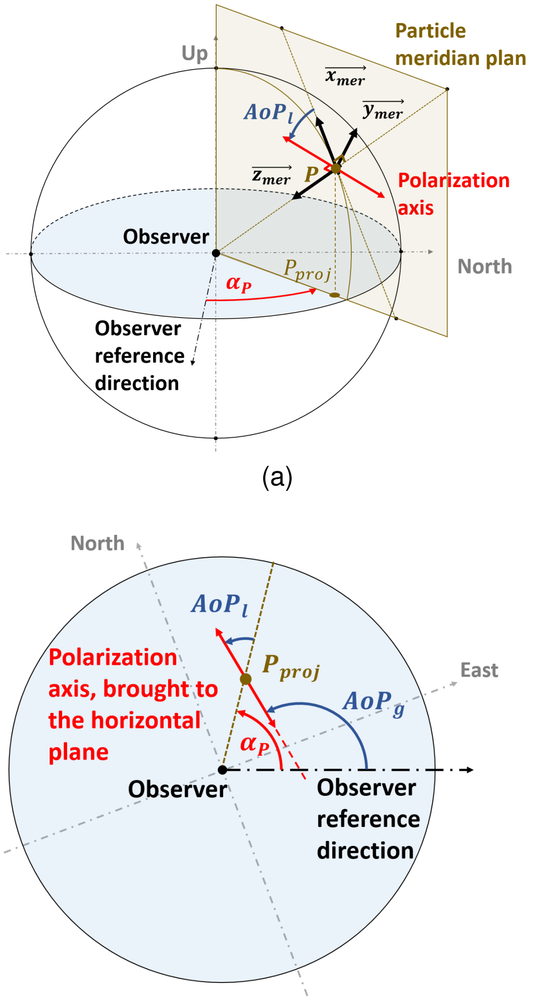

(a)

(b)

Fig. 5. Definitions of polarization angles AoP_l and AoP_g. (a) The local angle of polarization AoP_l is defined in a frame related to the particle point P with respect to the meridian plan. (b) The global angle of polarization AoP_g is defined with respect to the observer reference direction.

It is noteworthy that we chose to define the AoP_l backward regarding a (Fig. 1a). Indeed, in the example in Fig. 5, the AoP_l is near +45°, when it should be −45° referring to Poincaré formalism. We made this choice in order to make it easier to express the AoP in the observer frame.

V. NEUTRAL POINTS AND BERRY MODEL

The Rayleigh scattering model is broadly used but it only describes a single scattering phenomenon. In the Rayleigh scattering model, there are two points featuring null $DoLP$, the sun direction and the anti-sun direction. It has been shown [47], [48] that, due to atmospheric turbidity and multiple scattering, the global polarization pattern does not correspond to Rayleigh's model and that there are actually four points featuring null $DoLP$, which are called neutral points. As shown in Fig. 6, these four neutral points are named Brewster (below the sun), Babinet (above the sun), Arago (above the anti-sun) and the Fourth (below the anti-sun). They are all located on the solar meridian, but, for a fixed sun position, their respective elevations vary with the wavelength of light [47], [48] and the level of atmospheric turbidity, caused by air pollution, clouds, and even debris from volcanic eruptions [49], [50]. It also has been observed that distances between neutral points increase as the sun goes down [38], which could be easily intuited by the fact that the lower the sun in the sky, the thicker layer of the atmosphere and thus greater the scattering.

Berry suggested an enhanced model [28] to express AoP and $DoLP$ to account for the four observed neutral points. This model, more accurate than the Rayleigh model, can be useful for better heading measurements [51] but cannot be used as a pattern prediction model because the variations in the positions of neutral points are very difficult to predict.

It is worth noting that other models are available to more precisely compute skylight polarization than Rayleigh model, such as those relying on Mie scattering and Monte-Carlo based algorithms [52], which require considerable calculation resources.

The Berry model assumes that the Brewster and Babinet points are equidistant from the sun axis and are symmetric, about the observer point with, respectively, Arago and the Fourth points (Fig. 6). This model relies on the stereoscopic projection of the celestial unit sphere on its equator plane. The latter, centered on the observer, is considered as a complex plane, with the sun vector projected on the positive imaginary axis $i\Re^+$ (Fig. 7). Once the whole sky dome is projected onto this complex plane, the polarization parameters can be computed using a single function w defined in (15).

To compute the stereographic projections of the sky dome it is easier to use the zenith angles, as follows:

$$\begin{aligned} \varphi_p &= \tfrac{\pi}{2} - \theta_p \\ \varphi_s &= \tfrac{\pi}{2} - \theta_s \end{aligned} \tag{12}$$

As shown in Fig. 6, considering the sun vector is projected onto the positive imaginary axis, the four neutral point projections can be expressed as:

$$\begin{cases} Brewster_{proj} = \xi_+ = \mathrm{i} \cdot \frac{\tan(\frac{\varphi_s}{2})+\tan(\frac{\delta}{4})}{1-\tan(\frac{\theta_s}{2})\cdot\tan(\frac{\delta}{4})} \\ Babinet_{proj} = \xi_- = \mathrm{i} \cdot \frac{\tan(\frac{\varphi_s}{2})-\tan(\frac{\delta}{4})}{1+\tan(\frac{\theta_s}{2})\cdot\tan(\frac{\delta}{4})} \\ Arago_{proj} = -\frac{1}{\xi_+^*} \\ Fourth_{proj} = -\frac{1}{\xi_-^*} \end{cases} \tag{13}$$

Then for each particle in the sky dome, we have P_{proj} the stereographic projection of the particle point P as follows (Fig. 7):

$$P_{proj} = \xi = \tan(\frac{\varphi_p}{2}) \cdot \mathrm{e}^{\mathrm{i}\cdot(\alpha_p - \alpha_s + \frac{\pi}{2})} \tag{14}$$

Since we have the whole sky dome and the neutral points projections we can, as previously indicated, compute the whole polarization pattern with the Berry complex function w defined as follows:

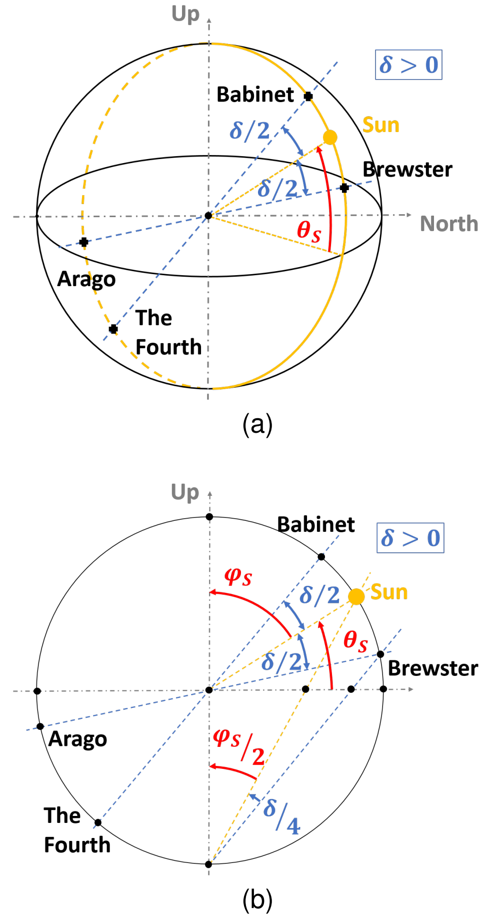

Fig. 6. Neutral Point positions according to the Berry model. (a) 3D view, (b) 2D view in the solar meridian plane.

$$\begin{cases} w : \xi \rightarrow w(\xi) \\ w(\xi) = -\frac{4\cdot(\xi-\xi_+)\cdot(\xi-\xi_-)\cdot(\xi-[-\frac{1}{\xi_+^*}])\cdot(\xi-[-\frac{1}{\xi_-^*}])}{(1+|\xi|^2)^2\cdot|\xi_+ + \frac{1}{\xi_+^*}|\cdot|\xi_- + \frac{1}{\xi_-^*}|} \end{cases} \tag{15}$$

This complex function carries in its modulus and phase, the intensity of polarization and the angle of polarization, respectively. Indeed $w(\xi)$ verifies (16).

$$\begin{cases} AoP_{g_{Berry}}(\xi) = \frac{1}{2} \cdot \mathrm{angle}(w(\xi)) \\ AoP_{g_{Berry}}(\xi) = 0 \text{ for polarization along } i\Re \text{ axis} \\ \\ IoP(\xi) = |w(\xi)| \\ 0 \leq IoP(\xi) \leq 1 \end{cases} \tag{16}$$

$IoP(\xi)$ is the intensity of polarization, which, based on the Brewster definition [29] is (17), with γ_+ and γ_- the angles between the observed direction and Brewster and Babinet points, respectively.

$$IoP(\xi) = |\sin(\gamma_+) \cdot \sin(\gamma_-)| \tag{17}$$

This definition of IoP does correspond to $I_{scat_{pol}}$ normalized (see (4) and (5)). It is worth noting that the polarization pattern of the Berry model corresponds exactly to the merging of two polarization patterns from the Rayleigh

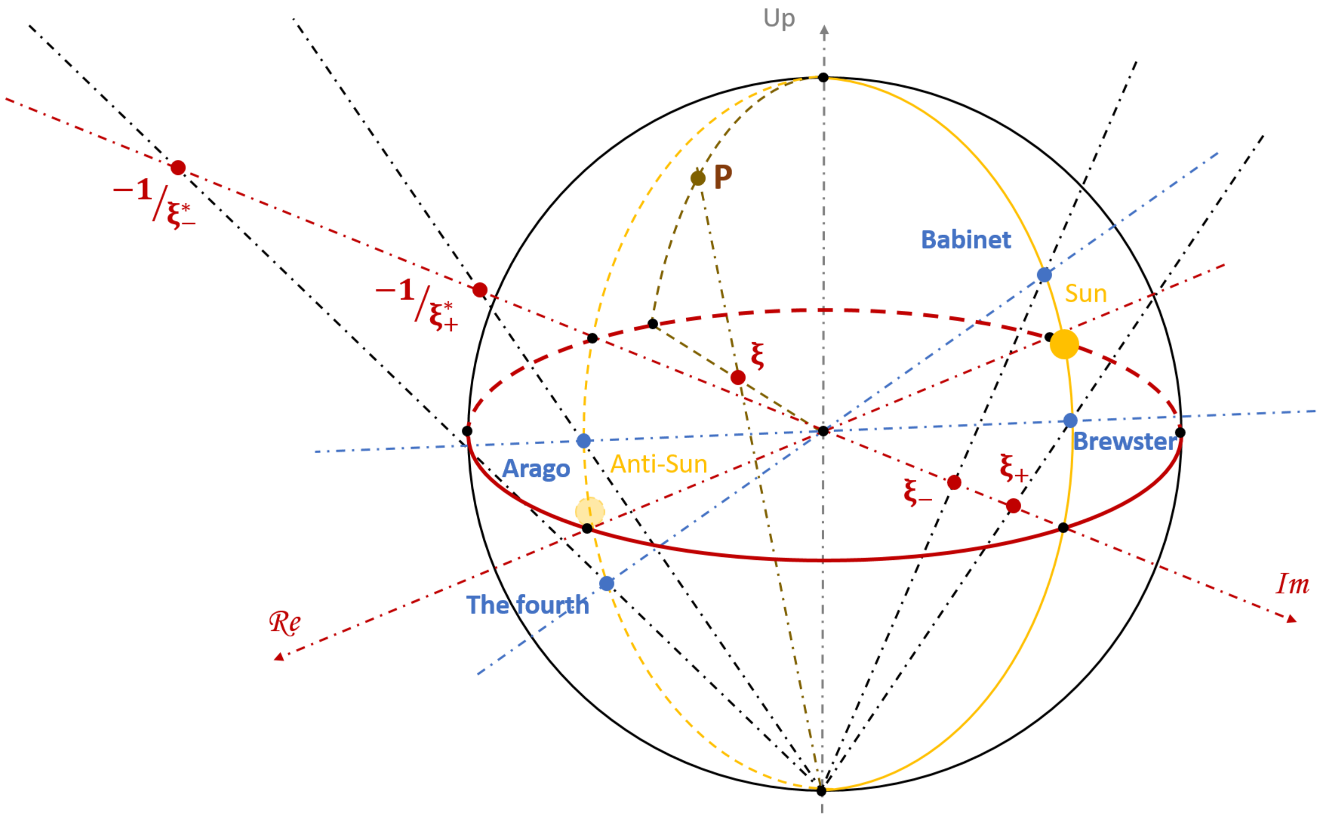

Fig. 7. Stereographic projection of the sky dome on its equator plane according to Berry model. The equator plane is seen as a complex plane with positive imaginary axis oriented toward the sun projection.

model. Indeed, considering γ_+ and γ_- as scattering angles we can obtain the polarization pattern from the Berry model by computing a first Rayleigh polarization pattern with the sun at the Babinet point position and a second Rayleigh polarization pattern with the sun at the Brewster point position, then compute each polarization angles (AoP) value as the arithmetic mean of the two AoP of the Rayleigh models and each intensity of polarization (IoP) value as the geometric mean of the two IoP of the Rayleigh models.

In this study, we adapted the Berry model to our observer frame, our AoP_g definition, and defined its associated $DoLP$ in order to make it fit with Rayleigh's. We computed the sky dome projection as explained in (18) and obtained the polarization parameters as explained in (19). In this last model the $\Re^+$ axis corresponds to the observer reference direction and, if we consider that $\delta = 0$, then the polarization pattern will correspond exactly to the polarization pattern of the Rayleigh model.

$$\begin{cases} P_{proj} = \xi = \tan(\frac{\varphi_p}{2}) \cdot \mathrm{e}^{\mathrm{i}\cdot\alpha_p} \\ Brewster_{proj} = \xi_+ = \mathrm{e}^{\mathrm{i}\cdot\alpha_s} \cdot \frac{\tan(\frac{\varphi_s}{2})+\tan(\frac{\delta}{4})}{1-\tan(\frac{\theta_s}{2})\cdot\tan(\frac{\delta}{4})} \\ Babinet_{proj} = \xi_- = \mathrm{e}^{\mathrm{i}\cdot\alpha_s} \cdot \frac{\tan(\frac{\varphi_s}{2})-\tan(\frac{\delta}{4})}{1+\tan(\frac{\theta_s}{2})\cdot\tan(\frac{\delta}{4})} \\ Arago_{proj} = -\frac{1}{\xi_+^*} \\ Fourth_{proj} = -\frac{1}{\xi_-^*} \end{cases} \tag{18}$$

$$\begin{cases} AoP_g(\xi) = \frac{1}{2} \cdot \mathrm{angle}(w(\xi) \cdot \mathrm{e}^{-2\cdot\mathrm{i}\cdot\alpha_s}) \\ AoP_g(\xi) = 0 \text{ for polarization along } \Re \text{ axis} \\ \\ DoLP(\xi) = \frac{|w(\xi)|}{2-|w(\xi)|} \end{cases} \tag{19}$$

As described in [28], in the standard Berry model, neutral point positions are symmetrical across the solar - anti-solar axis. By referring to Horvath's measurements [47], we can observe that this symmetrical property is not respected, indeed neutral points are placed along the solar meridian, but are not symmetrical with respect to the sun axis. We also observed this non-symmetrical distribution of the neutral points while testing our simulator and confronted it with real sky observations (see section X), especially under very cloudy skies.

An interesting point would be to break these symmetries between the Brewster and Babinet neutral points and between the Arago and Fourth neutral points on purpose. In this study, we chose to use independent neutral point positions with regards to the sun elevation and keep the complex conjugation between them, which is equivalent to keeping the standard Berry model with a false sun elevation. In a previous study [53], the choice was made to keep the standard Berry model except for the symmetry around the anti-sun half axis only, another possibility would be to give all neutral points independent positions along the solar meridian. This breaking of the symmetry seems to be particularly relevant to simulate extremely cloudy skies with which we can observe, if we rely on the standard Berry model, what could be seen as a total loss of perception of the sun elevation (see section X and Fig. 11), indeed the polarization pattern acts as if the sun was stuck at the zenith or the horizon.

Another option to modify the Berry model would be to implement weight coefficients in the arithmetic and geometric means, of respectively AoP and IoP, involved in the w function's construction in order to influence each singularity's (neutral point) impact on the polarization pattern.

VI. RADIANCE MODEL OF THE SKY

A complete simulation of light polarization measurements of the celestial dome must include a model of sky radiance. This allows the simulation to take account of possible sensor saturation phenomenon and low signal-to-noise ratio which would affect AoP and $DoLP$ patterns' measurements. As with the approach described in previous studies [31]–[34], ours consists of using the CIE luminance model which describes sky luminance distribution across different cloud conditions, depending on sun elevation. Using a photometric model rather than a radiometric one may initially appear a strange choice but we did so because both monochromatic cameras and RGGB cameras are made to fit the human eye spectral sensitivity, this allows the CIE model to produce faithful radiance seen by standard sensors, except for a proportionality constant.

The CIE luminance model gives the sky dome luminance distribution as a function of the observed direction's zenith angle φ_p, the sun's zenith angle φ_s, the scattering angle γ (defined positive) and the five following coefficients:

A: horizon-zenith gradient, from -5 to $+5$

B: gradient intensity, from -10 to 0

C: circumsolar intensity, from 0 to $+25$

D: circumsolar radius, from -10 to 0

E_{CIE}: backscattering effect, from -1 to $+5$

As used in [31]–[34], the CIE luminance gives the absolute sky luminance, but in our model, we are only interested in relative luminance, (or relative radiance) coming to our sensor device regarding its own saturation illuminance (or irradiance). That is why, we only used the relative luminance distributions in (20) and implemented a pixel saturation-ratio in order to take account of sensor saturation effects due to the sensor's sensitivity and exposure (see section VIII). The relative luminance distribution in (20) is defined such that the luminance value at zenith is always 1.

To simulate different sky luminance distributions, within our simulator, we implemented the 15 standard skies of the CIE luminance model, described in table II.

This relative luminance model has not been designed to calculate luminance below the horizon.

$$L_{rel} = \frac{1 + A \cdot \mathrm{e}^{B/\cos(\varphi_p)}}{1 + A \cdot \mathrm{e}^{B}} \cdot \frac{1 + C \cdot (\mathrm{e}^{D\gamma} - \mathrm{e}^{D\pi/2}) + E_{\text{CIE}} \cdot \cos^2(\gamma)}{1 + C \cdot (\mathrm{e}^{D\varphi_s} - \mathrm{e}^{D\pi/2}) + E_{\text{CIE}} \cdot \cos^2(\varphi_s)} \tag{20}$$

VII. OPTICAL MODEL OF OBJECTIVE LENS

We wanted our simulator to be able to deal with thin lenses, fisheye lenses and their associated fields of view, so we implemented an optical model able to simulate various infinity-focus optical conjugations. This model is composed of the thin lens model and the four standard fisheye conjugation models [35], which correspond to standard off-the-shelf fisheye lenses. Each of the four fisheye conjugation models has an interesting geometric property for imaging: the first performs a stereographic projection of the field of view, the fourth an orthogonal projection of the field of view, the second preserves proportionality between angles and the third between solid angles in the image field.

Considering a lens of focal length f with an object at infinity of angle θ, as in Fig. 8a, there are five ways to compute $r(\theta)$, the distance between the optical axis and the image point of the object in our model. We named those five possible r computations r_0, r_1, r_2, r_3 and r_4:

$$\begin{cases} r_0(\theta) = f \cdot \tan(\theta) \text{ (thin lens)} \\ \\ r_1(\theta) = 2 \cdot f \cdot \tan(\frac{\theta}{2}) \text{ (stereographic projection)} \\ r_2(\theta) = f \cdot \theta \text{ (equi angle imaging)} \\ r_3(\theta) = 2 \cdot f \cdot \sin(\frac{\theta}{2}) \text{ (equi solid angle imaging)} \\ r_4(\theta) = f \cdot \sin(\theta) \text{ (orthogonal projection)} \end{cases} \tag{21}$$

Those five r computations verify the partial order relation (22). Figure 8b shows how convergent each model is compared to others by geometrical construction for an object of significant angular size.

$$|r_0| > |r_1| > |r_2| > |r_3| > |r_4| \tag{22}$$

In our simulator, we use a single lens model, without image reversal effect, to simulate the whole objective lens placed above the imager. In a real objective, in order to correct optical aberrations, there is more than one lens in the optical system. Considering this, for a camera looking toward the zenith, each point on the sky dome sphere of azimuth α_p and zenith angle ϕ_p is imaged on a sensor centered in the observer point at the coordinates $(r(\phi_p) \cdot \cos(\alpha_p), r(\phi_p) \cdot \sin(\alpha_p))$

We only consider optical conjugation and do not take into account the minor polarization disturbance due to refraction in the optical system. There is no polynomial computation of distortion either. It could be possible to improve our model by implementing a new function which would use Mueller matrix, previously estimated experimentally, to increase the fidelity of optical model.

VIII. POLARIZERS AND SENSOR MODEL

We chose for our simulator to implement an imaging sensor with micro polarizers array upstream, just like the IMX250MZR model from SONY, which is one of the two sensors set on the two cameras we used for our outdoor experiments.

This kind of polarimetric imager is composed of a micropolarizers array substrate, arranged such that each block of four pixels faces four linear polarizers oriented in four different

TABLE II
CIE STANDARD SKIES.

CIE standard skies and coefficients						
	Skies description	A	B	C	D	E_{CIE}
1	CIE standard overcast sky, steep luminance gradation towards zenith azimuthal uniformity	4.0	-0.7	0	-1	0
2	Overcast, with steep luminance gradation and slight brightening towards the sun	4.0	-0.7	2	-1.5	0.15
3	Overcast, moderately graded with azimuthal uniformity	1.1	-0.8	0	-1	0
4	Overcast, moderately graded and slight brightening towards the sun	1.1	-0.8	2	-1.5	0.15
5	Sky of uniform luminance	0	-1	0	-1	0
6	Partly cloudy sky, no gradation towards zenith, slight brightening towards the sun	0	-1	2	-1.5	0.15
7	Partly cloudy sky, no gradation towards zenith, brighter circumsolar region	0	-1	5	-2.5	0.3
8	Partly cloudy sky, no gradation towards zenith, distinct solar corona	0	-1	10	-3	0.45
9	Partly cloudy, with the obscured sun	-1	-0.55	2	-1.5	0.15
10	Partly cloudy, with brighter circumsolar region	-1	-0.55	5	-2.5	0.3
11	White-blue sky with distinct solar corona	-1	-0.55	10	-3	0.45
12	CIE standard clear sky, low luminance turbidity	-1	-0.32	10	-3	0.45
13	CIE standard clear sky, polluted atmosphere	-1	-0.32	16	-3	0.3
14	Cloudless turbid sky with broad solar corona	-1	-0.15	16	-3	0.3
15	White blue turbid sky with broad solar corona	-1	-0.15	24	-2.8	0.15

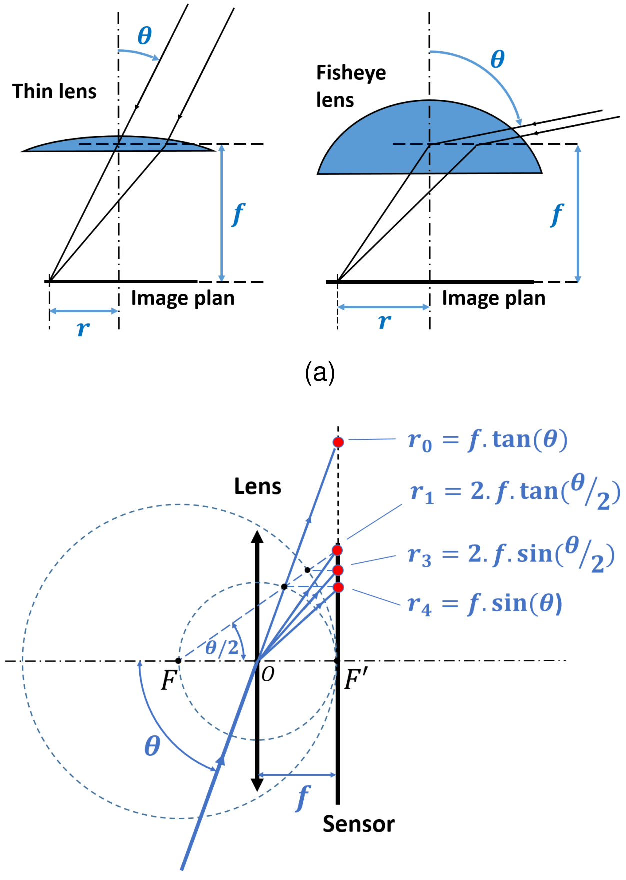

(a)

(b)

Fig. 8. Various types of infinity-focus conjugations depending on lens models. (a) Thin lens $vs.$ fish-eye lens. (b) r_0, r_1, r_3, and r_4 geometric construction for the same focal length f and same angle of object at infinity θ. F and F' are the image and focal points, O is the center of the lens.

directions: 0°, 45°, 90° and 135° in the $\overrightarrow{X_{sensor}}$, $\overrightarrow{Y_{sensor}}$ plan (Fig. 9).

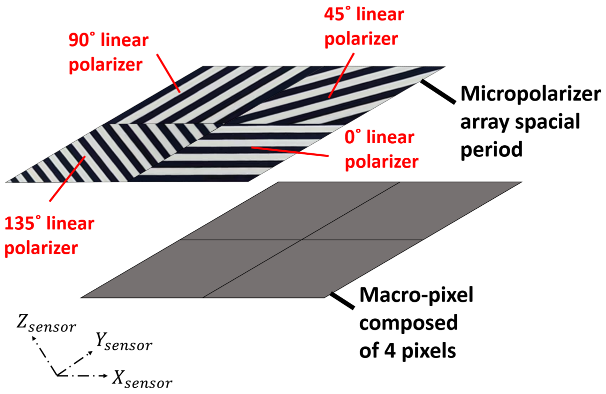

Fig. 9. A macro-pixel of the polarimetric camera is composed of four individual pixels and four polarized filters oriented in four different directions: 0°, 45°, 90° and 135°. In our simulator Z_{sensor} is the up axis and X_{sensor} is the observer reference direction.

Those sensors were designed to easily compute the first three Stokes parameters. For each macro-pixel, the global angle of polarization AoP_g and the degree of linear polarization $DoLP$ can be computed as follows:

$$\begin{cases} S_0 = \frac{I_0+I_{90}+I_{45}+I_{135}}{2} \\ S_1 = I_0 - I_{90} \\ S_2 = I_{45} - I_{135} \\ \\ DoLP = \frac{\sqrt{S_1^2+S_2^2}}{S_0} \\ AoP_g = 0.5 \cdot \arg(S_1 + \mathrm{i} \cdot S_2) \end{cases} \tag{23}$$

We simulated the polarimetric sensor using two different functions. The first function describes the micropolarizer array using (25) and (26), and the second function describes the conversion from light power to digital grayscale of the pixel array using (27).

Considering total light intensity entering a micropolarizer I_{in}, the transmittance for an incident beam which is totally linearly polarized along transmission axis T_1 , the transmittance for an incident beam which is totally linearly polarized at 90°

from transmission axis T_2, the angle between the transmission axis of the micropolarizer and the observer reference direction ψ, we can then compute the light intensity at the output of the micropolarizer I_{out} by decomposing the light into polarized and unpolarized components as follows:

$$\begin{aligned} I_{out} = I_{in} \cdot (1 - DoLP) \cdot \frac{1}{2} \cdot (T_1 + T_2) \\ + I_{in} \cdot DoLP \cdot \cos^2(AoP_g - \psi) \cdot T_1 \\ + I_{in} \cdot DoLP \cdot \cos^2(AoP_g - \psi - \frac{\pi}{2}) \cdot T_2 \end{aligned} \quad (24)$$

In a simplified way, with $\varepsilon = (T_1 - T_2)/(T_1 + T_2)$ being the polarization efficiency of polarizers [54], we get:

$$\frac{I_{out}}{T_1 + T_2} = \frac{I_{in}}{2} \cdot (1 + DoLP \cdot \varepsilon \cdot \cos(2AoP_g - 2\psi)) \quad (25)$$

In this study, as we use relative light intensity without considering absorbance, we assume that the sum of T_1 and T_2 is equal to 1.

To take account of the mechanical error in the polarizers' orientations, we add an angular random uniform noise $\Delta\psi$.

$$\psi = \psi_{\text{perfect}} + \Delta\psi \quad (26)$$

After computing the light intensity coming through the polarizer array, the last step is to compute the pixel array's digital grayscale output. To do so, we use only three parameters: a Gaussian noise of signal-to-noise ratio SNR, a pixel saturation ratio R_{sat} and the number of bits N_{bit} of the quantizer used to convert the light intensity into an integer. What we call "Pixel saturation ratio" is the ratio of the pixel saturation light intensity to the maximum light intensity arriving at the pixel array ($I_{out_{max}}$). This gives the final output signal for each pixel:

$$\begin{aligned} P_{\text{output}} = \min(2^{N_{bit}} - 1, \\ \left\lfloor (2^{N_{bit}} - 1) \cdot \frac{I_{out}(1 + \Delta G/\text{SNR})}{I_{out_{max}} \cdot R_{sat}} \right\rfloor) \end{aligned} \quad (27)$$

with ΔG a random Gaussian noise.

IX. SIMULATOR ARCHITECTURE

Our simulator, described in Fig. 10, relies on six functions (gray blocks in Fig. 10), each of which is based on the theoretical models described in sections III to VIII. It takes, as simulated measurement input parameters, the sensor's pixel array dimensions, the characteristics of used optics, the sun position, the type of observed sky, the sky turbidity using the angle δ of the previously presented Berry model, the micro-polarizers' efficiency and orientation error, the sensor dynamics characteristics and returns the polarimetric camera output image.

We added a seventh function, named Simu_Data_Processing, to process the output data of the simulated polarimetric camera and the data collected by real polarimetric cameras during our outdoor experiments, in order to facilitate the image comparison between simulation and ground truth. This seventh function simply returns the $DoLP$, AoP_g and AoP_l using (23) and (11).

To display the polarization pattern in our Matlab code version, we used circular color maps described by P. Kovesi [55], which are very useful in displaying angular values of the AoP.

Each function of our simulator can easily be changed or upgraded, and transforming the intermediate data (purple blocks in Fig. 10) by adding new functions is also straightforward, for example, it is not difficult to tilt the sensor plane by applying an inverse rotation matrix to visual field data.

X. EXPERIMENTAL DATA VS SIMULATIONS

In this section, we compare images generated by OpenSky with experimental data obtained under various weather conditions. We used two different polarimetric cameras equipped with two different optics. Those cameras were used in two distinct places in Marseille (France). The first is a monochromatic camera, with a horizontal half-field of view of 27.8° (Fig. 11, Table III and Fig. 12, Table IV), and the second is a RGGB fisheye camera with a horizontal half-field of view of 90° (Fig. 13, Table V and Fig. 14, Table VI).

During outdoor experiments, real camera pictures were captured in ".tiff" format. We just read those pictures as 16-bit integer matrices and applied the exact same image processing function to both outdoor camera images and OpenSky generated images. An example of a comparison between real and simulated images can be found in the GitHub repository, based on one of our camera capture included in the repository.

Each of these cameras provided raw image data that we subsequently simulated afterwards, using the Berry model. Both raw and simulated images were then processed with the same image processing algorithm relying on (23) and (11).

To simulate sky polarization measurement, we had looked up the sun position with respect to the orientation of the cameras by using an algorithm developed for solar radiation applications, computing solar ephemeris [56].

As explained in section V, we can observe in Fig. 11 and Table III, for extremely cloudy skies, what we can call a "loss of perception of the sun elevation" relying on the standard Berry model, or a loss of symmetry of the neutral points regarding the sun-observer axis. To simulate overcast sky observation, we found that we have to voluntarily introduce a breaking of the symmetry in the positions of the neutral points. We achieved this by using a false sun elevation for polarization pattern simulation with the Berry model (see parameters "sun elevation" and δ in Table III).

Concerning the fisheye measurement simulation, because the CIE model equation (20) is not made to be relevant for sky elevation under the horizon and could compromise computation, we used a binary mask on relative luminance results for our simulated data (Figs. 13 and 14), setting to zero all luminance coming from under the horizon.

After developing our simulator, we also used it to test some preliminary results of the Skypole method [25].

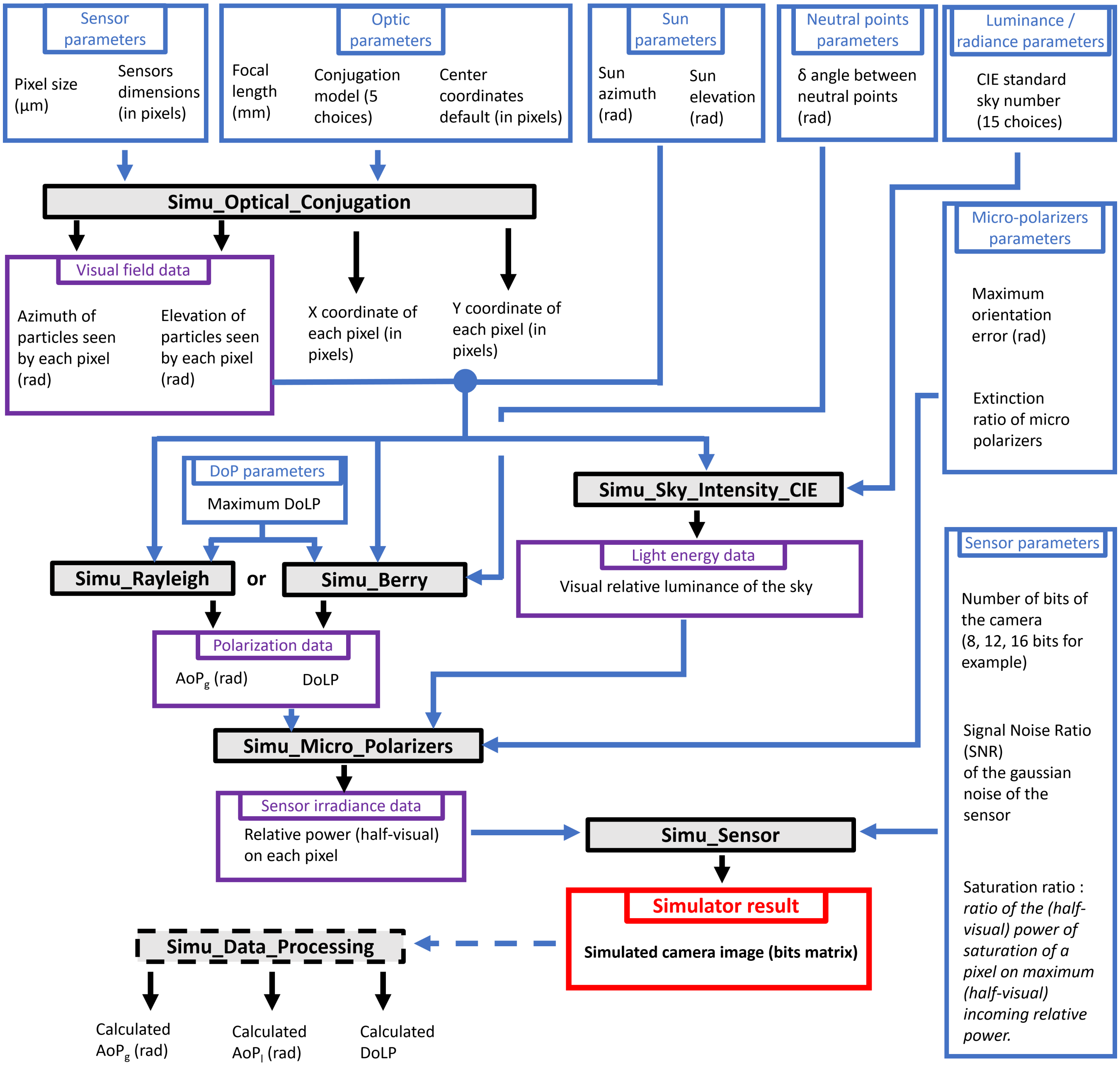

Fig. 10. Modular architecture of the OpenSky simulator. Each set of parameters and functions are clearly separated in order to make the simulator as generic as possible and user-friendly. Input parameters are in blue edged boxes, in the upper right part, intermediate parameters are in purple edge boxes, functions are in gray colored boxes and the final result is in the red box in the lower middle area.

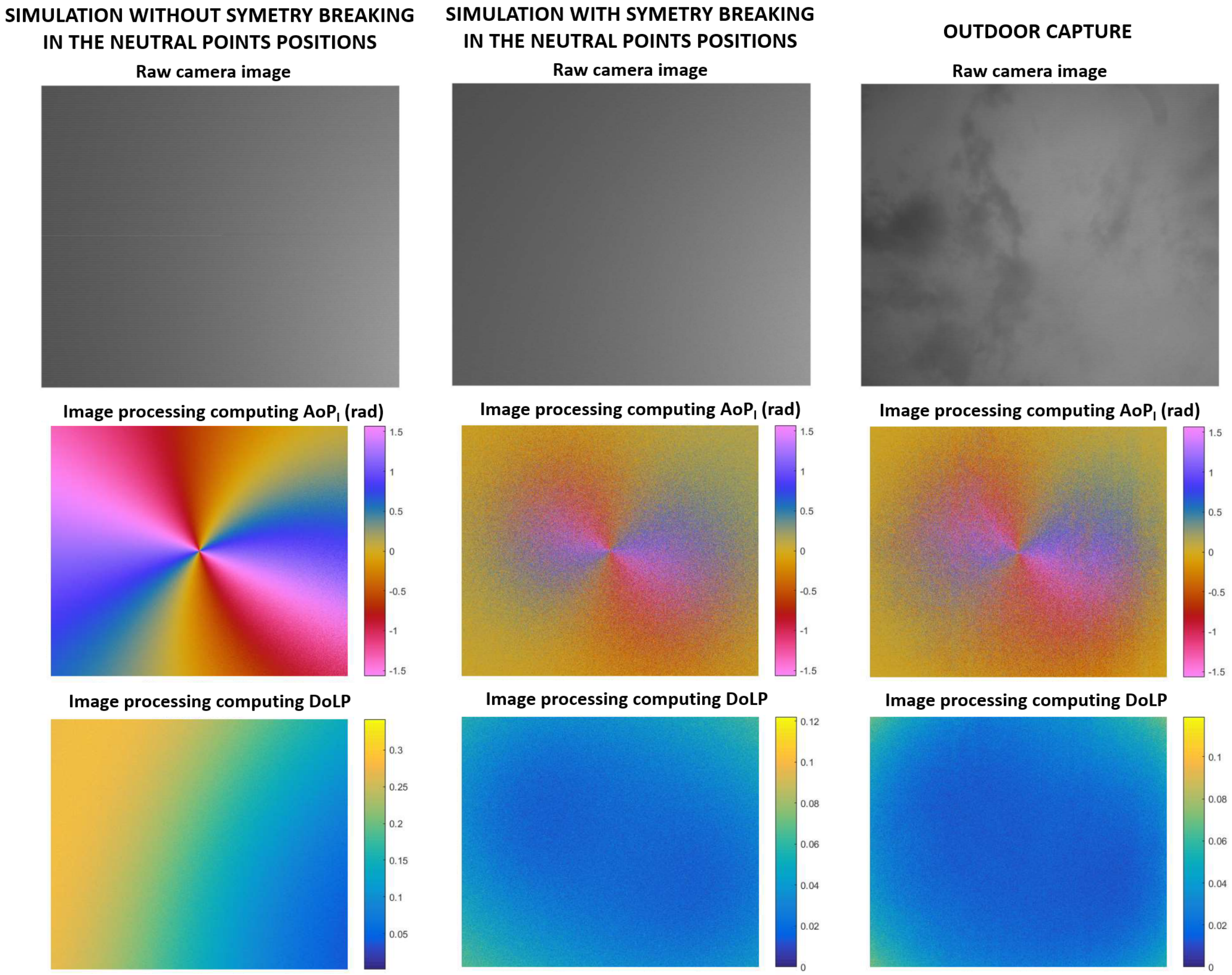

SIMULATION WITHOUT SYMETRY BREAKING IN THE NEUTRAL POINTS POSITIONS

SIMULATION WITH SYMETRY BREAKING IN THE NEUTRAL POINTS POSITIONS

OUTDOOR CAPTURE

Raw camera image

Image processing computing AoP_l (rad)

Image processing computing DoLP

Fig. 11. Measurements and simulations in very cloudy conditions with a thin lens objective camera. From top to bottom: the camera image, the calculated local angle of polarization AoP_l, the calculated degree of linear polarization $DolP$. From left to right: the standard simulation with neutral points close to each other around sun and anti-sun positions, the simulation with widely spaced neutral points which do not follow the expected symmetry from the Berry model, and the outdoor experiment. The measurement took place at lat $43.2337929°$ N, long $5.4441861°$ E, October 20, 2022 at 03:30pm (local hour, timezone +2h).

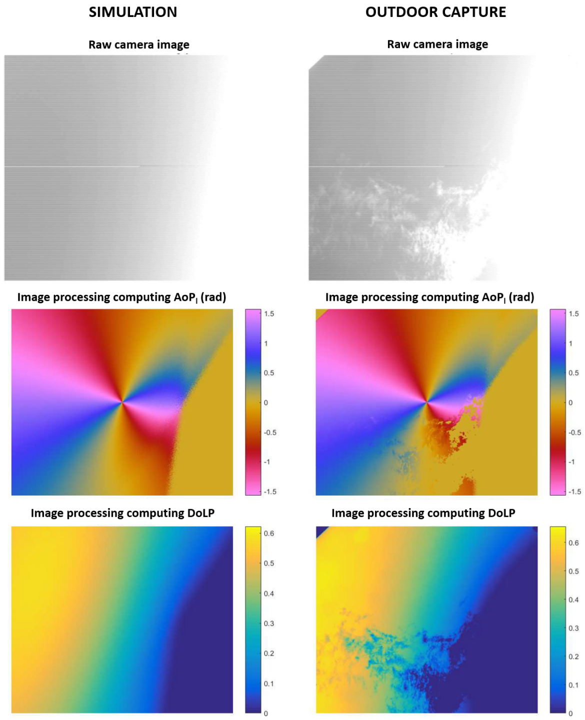

Fig. 12. Measurement and simulation for clear sky with a few thin clouds with a thin lens objective camera. From top to bottom: the camera image, the calculated AoP_l, the calculated $DolP$. From left to right: the simulation, the outdoor experiment. The measurement was taken at lat $43.2337929°$N, long $5.4441861°$E, January 25, 2023 at 11:33am (local hour, timezone +1h)

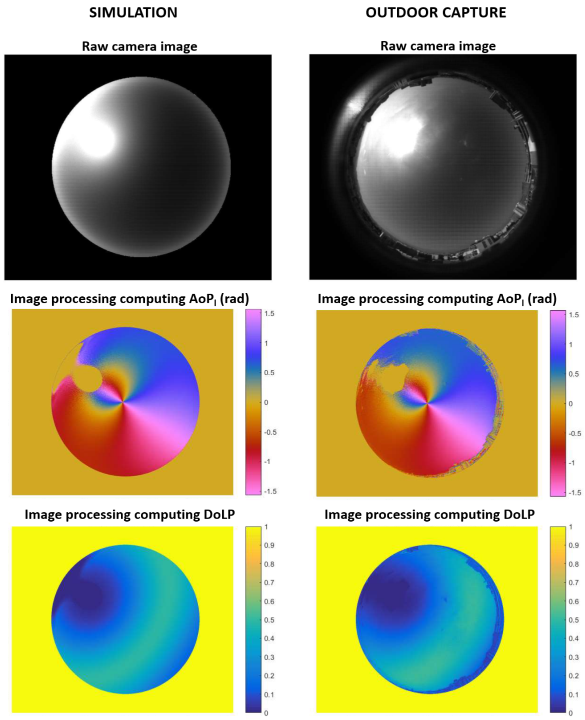

Fig. 13. Measurement and simulation for sky with thin clouds with a fisheye camera. From top to bottom: the camera image, the calculated AoP_l, the calculated $DolP$. From the left to the right: the simulation, the outdoor experiment. The measurement was taken at lat $43.2869904°$N, long $5.4033614°$E, July 12, 2022 at 10:30am (local hour, timezone +2h)

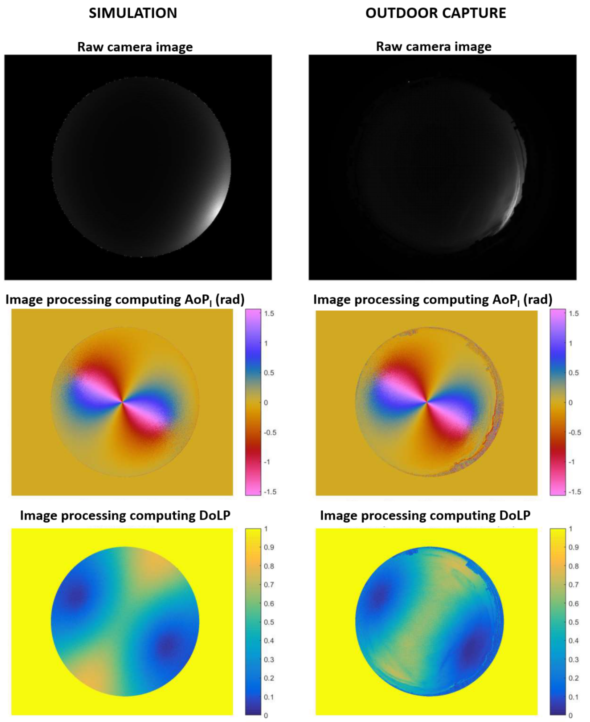

Fig. 14. Measurement and simulation for clear sky with a fisheye camera. From top to bottom: the camera image, the calculated AoP_l, the calculated $DolP$. From left to right: the simulation, the outdoor experiment. The measurement was taken at lat 43.2869904°, long 5.4033614°, August 26, 2022 at 08:30pm (local hour, timezone +2h)

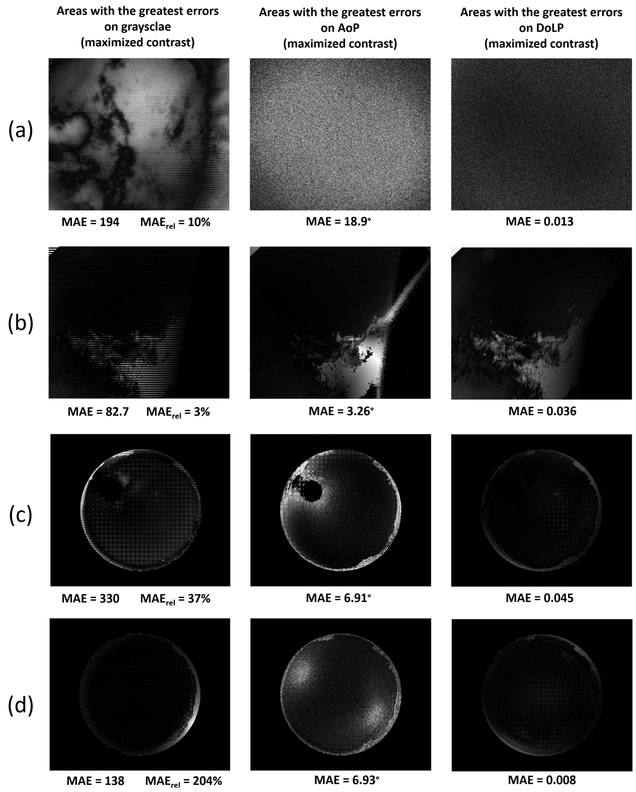

Fig. 15. Comparisons between measurement and simulation. Each picture shows the absolute difference between simulation and measurement, the differences are normalized so that their biggest values are always 1. From the left to the right, normalized differences between the shades of gray of raw images (simulated and real), normalized differences between AoP values after image processing, normalized differences between $DoLP$ values after image processing. (a), (b), (c) and (d) correspond respectively to the measurements from October 20, 2022, January 25, 2023, July 12, 2022 and August 26, 2022, previously presented. The grayscale dynamic is $[0, 4095]$. The MAE_{rel} is the mean of the ratio of the absolute error on simulated shades of gray with the measured shades of gray. The relatively high MAE_{rel} on (c) and (d) is due to the use of an RGB camera instead of a monochromatic camera in (a) and (b) leading to an important local variation of the gray level.

Despite a satisfactory visual aspect to the OpenSky images shown in Figs. 11-14 we used a metric to quantify the distance between outdoor camera captures and simulator generated images. We used a standard method to characterize our simulator using the Mean Average Error (MAE) applied on grayscale pictures [57]. Figure 15 shows a comparison between simulated and real grayscale images, and between their extracted AoP and DoP, shown in Figs. 11-14. A second method, which would possibly make it possible to better estimate the reliability of OpenSky, would consist of training different image processing algorithms, twice each, both from an image bank provided by OpenSky and from a database of images obtained from real observations of the sky, separately. Then, for each image processing algorithm, performance under real outdoor conditions would be compared between the version trained from real data and the version trained from simulated data. Simulator reliability would be measured through the uniformity between the performance distribution of algorithms trained in simulation and the performance distribution of algorithms trained in outdoor capture.

XI. CONCLUSION

In this study, a complete simulator is presented for yielding faithful polarized patterns of the sky measured by a polarimetric camera in various cloudy conditions. This simulator outputs raw camera images that can be further processed by other algorithms (e.g. angle and degree of polarization patterns extractor). OpenSky is modular and structured so as to be user-friendly in terms of parameter settings and the insertion of additional blocks. OpenSky is an open source simulator available in both Python and Matlab formats at https://github.com/MoutenetA/OpenSky and https://osf.io/rynv7/?view_only=13674c69c28148879f96dd472db11e2e. OpenSky can be easily adjusted by modifying a few parameters to account for the disparity that exists between all types of skies. In addition, future improvements could be added. For example, possible Mueller matrices could be used to describe the polarizing effect of optics on measurements, or simulation blocks for other optical devices like waveplates could be added. In further studies, we will show that OpenSky could be used as a proxy for developing new polarization-based algorithms by training neural networks with simulated polarimetric images and validating those networks with real images.

OpenSky could help in the design of future optical sensors and image processing software for measuring absolute heading or to implement global positioning methods by using polarized images. Finally, OpenSky is the first step for simulators able to provide both high fidelity patterns of polarized skylight and reliable images, making this tool an ideal companion for future developments of visual processing algorithms.

REFERENCES

[1] C. Evangelista, P. Kraft, M. Dacke, T. Labhart, and M. Srinivasan, "Honeybee navigation: critically examining the role of the polarization compass," Philosophical Transactions of the Royal Society B: Biological Sciences, vol. 369, no. 1636, p. 20130037, 2014.

[2] R. Wehner, Desert navigator: the journey of an ant. Harvard University Press, 2020.

[3] M. Dacke and B. El Jundi, "The dung beetle compass," Current Biology, vol. 28, no. 17, pp. R993–R997, 2018.

[4] S. Heinze, S. Gotthardt, and U. Homberg, "Transformation of polarized light information in the central complex of the locust," Journal of Neuroscience, vol. 29, no. 38, pp. 11 783–11 793, 2009.

[5] S. M. Reppert, H. Zhu, and R. H. White, "Polarized light helps monarch butterflies navigate," Current Biology, vol. 14, no. 2, pp. 155–158, 2004.

[6] T. Labhart and E. P. Meyer, "Detectors for polarized skylight in insects: a survey of ommatidial specializations in the dorsal rim area of the compound eye," Microscopy research and technique, vol. 47, no. 6, pp. 368–379, 1999.

[7] B. J. Hardcastle, J. J. Omoto, P. Kandimalla, B.-C. M. Nguyen, M. F. Keleş, N. K. Boyd, V. Hartenstein, and M. A. Frye, "A visual pathway for skylight polarization processing in drosophila," Elife, vol. 10, p. e63225, 2021.

[8] M. L. Brines and J. L. Gould, "Skylight polarization patterns and animal orientation," Journal of Experimental Biology, vol. 96, no. 1, pp. 69–91, 1982.

[9] M. Belenkii, L. Sverdrup, and V. Kolinko, "Celestial compass with sky polarization," US Patent US20 150 042 793, 2013.

[10] E. Doucet, "Determination of attitude of a vehicle based on sky polarization by acelestial light source," DE Patent DE102 018 132 590, 2018.

[11] L. Poughon, S. Mafrica, J. Monnoyer, L. Pradere, J. Serres, and S. Viollet, "Procédé et système pour déterminer des données caractérisant un cap suivi par un véhicule automobile à un instant courant," fr Patent FR3 128 528, 2021.

[12] L. Guan, P. Zhang, H. Cai, L. Zhai, Y. Cui, and J. Chu, "Astronomical navigation ship position calculation method based on atmospheric polarization light field," CN Patent CN111 412 916B, 2020.

[13] F. Kong, Y. Guo, J. Zhang, X. Fan, and X. Guo, "Review on bio-inspired polarized skylight navigation," Chinese Journal of Aeronautics, 2023.

[14] Q. Zhang, J. Yang, X. Liu, and L. Guo, "A bio-inspired navigation strategy fused polarized skylight and starlight for unmanned aerial vehicles," IEEE Access, vol. 8, pp. 83 177–83 188, 2020.

[15] H. Liang, H. Bai, N. Liu, and X. Sui, "Polarized skylight compass based on a soft-margin support vector machine working in cloudy conditions," Applied Optics, vol. 59, p. 1271, 2020.

[16] L. M. Eshelman, A. M. Smith, K. M. Smith, and D. B. Chenault, "Unique navigation solution utilizing sky polarization signatures," in Polarization: Measurement, Analysis, and Remote Sensing XV, vol. 12112. SPIE, 2022, p. 1211203.

[17] Z. Cheng, T. Mei, and H. Liang, "Positioning algorithm based on skylight polarization navigation," IFAC Proceedings Volumes, vol. 46, no. 10, pp. 97–101, 2013.

[18] J. Yang, X. Liu, Q. Zhang, T. Du, and L. Guo, "Global autonomous positioning in gnss-challenged environments: A bioinspired strategy by polarization pattern," IEEE Transactions on Industrial Electronics, vol. 68, no. 7, pp. 6308–6317, 2020.

[19] Y. Wang, J. Chu, R. Zhang, L. Wang, and Z. Wang, "A novel autonomous real-time position method based on polarized light and geomagnetic field," Scientific reports, vol. 5, no. 1, p. 9725, 2015.

[20] J. Liu, J. Yang, Y. Wang, J. Tang, and C. Shen, "Global positioning method based on polarized light compass system," Review of Scientific Instruments, vol. 89, no. 5, p. 054503, 2018.

[21] Q. Zhang, J. Yang, P. Huang, X. Liu, S. Wang, and L. Guo, "Bionic integrated positioning mechanism based on bioinspired polarization compass and inertial navigation system," Sensors, vol. 21, no. 4, p. 1055, 2021.

[22] W. Stürzl and N. Carey, "A fisheye camera system for polarisation detection on uavs," in Computer Vision – ECCV 2012. Workshops and Demonstrations, A. Fusiello, V. Murino, and R. Cucchiara, Eds. Berlin, Heidelberg: Springer Berlin Heidelberg, 2012, pp. 431–440.

[23] C. Fan, X. Hu, X. He, L. Zhang, and J. Lian, "Integrated polarized skylight sensor and mimu with a metric map for urban ground navigation," IEEE Sensors Journal, vol. 18, no. 4, pp. 1714–1722, 2017.

[24] S. B. Powell, R. Garnett, J. Marshall, C. Rizk, and V. Gruev, "Bioinspired polarization vision enables underwater geolocalization," Science advances, vol. 4, no. 4, p. eaao6841, 2018.

[25] T. Kronland-Martinet, L. Poughon, M. Pasquinelli, D. Duché, J. R. Serres, and S. Viollet, "Skypole—a method for locating the north celestial pole from skylight polarization patterns," Proceedings of the National Academy of Sciences, vol. 120, no. 30, p. e2304847120, 2023.

[26] X. Bai, Z. Liang, Z. Zhu, A. Schwing, D. Forsyth, and V. Gruev, "Polarization-based underwater geolocalization with deep learning," eLight, vol. 3, no. 1, Jul. 2023.

[27] L. Guo, S. Wang, J. Yang, and X. Liu, "Autonomous positioning method based on polarization north pole and polarization sun vector," CN Patent CN110 887 477B, 2019.

[28] M. V. Berry, M. R. Dennis, and R. L. J. Lee, "Polarization singularities in the clear sky," New Journal of Physics, 2004.

[29] S. D. B. K. D. F. V. Edin., "Lxviii. on the polarization of the atmosphere," The London, Edinburgh, and Dublin Philosophical Magazine and Journal of Science, vol. 31, no. 210, pp. 444–454, 1847.

[30] S. Darula and R. Kittler, "Cie general sky standard defining luminance distributions," Proceedings eSim, vol. 11, p. 13, 2002.

[31] A. Wilkie, C. Ulbricht, R. F. Tobler, G. Zotti, and W. Purgathofer, "An Analytical Model for Skylight Polarisation," in Eurographics Workshop on Rendering, A. Keller and H. W. Jensen, Eds. The Eurographics Association, 2004.

[32] L. Hosek and A. Wilkie, "An analytic model for full spectral sky-dome radiance," ACM Transactions on Graphics, 2012.

[33] D. Li, C. Li, S. Lou, E. Tsang, and J. Lam, "Analysis of vertical sky components under various cie standardgeneral skies," Indoor and Built Environment, 2015.

[34] X. Wang, J. Gao, Z. Fan, and N. W. Roberts, "An analytical model for the celestial distribution of polarized light, accounting for polarization singularities, wavelength and atmospheric turbidity," Journal of Optics, vol. 18, no. 6, p. 065601, apr 2016.

[35] W. Hou, M. Ding, N. Qin, and X. Lai, "Digital deformation model for fisheye image rectification," Optics express, vol. 20, no. 20, pp. 22 252–22 261, 2012.

[36] F. F. Carvalho, C. A. de Moraes Cruz, G. C. Marques, and K. M. C. Damasceno, "Angular light, polarization and stokes parameters information in a hybrid image sensor with division of focal plane," Sensors, vol. 20, p. 3391, 2020.

[37] H. G. Berry, G. Gabrielse, and A. Livingston, "Measurement of the stokes parameters of light," Applied optics, vol. 16, no. 12, pp. 3200–3205, 1977.

[38] P. Pan, X. Wang, T. Yang, X. Pu, W. Wang, C. Bao, and J. Gao, "High-similarity analytical model of skylight polarization pattern based on position variations of neutral points," Opt. Express, vol. 31, no. 9, pp. 15 189–15 203, Apr 2023.

[39] Q. Li, L. Dong, Y. Hu, Q. Hao, J. Lv, J. Cao, and Y. Cheng, "Skylight polarization pattern simulator based on a virtual-real-fusion framework for urban bionic polarization navigation," Sensors, vol. 23, no. 15, 2023.

[40] H. Liang and H. Bai, "Polarized Skylight Navigation Simulation (PSNS) Dataset," arXiv, 2021.

[41] E. Gkanias, B. Risse, M. Mangan, and B. Webb, "From skylight input to behavioural output: a computational model of the insect polarised light compass," PLoS computational biology, vol. 15, no. 7, p. e1007123, 2019.

[42] T. Stone, B. Webb, A. Adden, N. B. Weddig, A. Honkanen, R. Templin, W. Wcislo, L. Scimeca, E. Warrant, and S. Heinze, "An anatomically constrained model for path integration in the bee brain," Current Biology, vol. 27, no. 20, pp. 3069–3085, 2017.

[43] H. Liang, H. Bai, K. Hu, and X. Lv, "Bioinspired polarized skylight orientation determination artificial neural network," Journal of Bionic Engineering, vol. 20, no. 3, pp. 1141–1152, 2023.

[44] T. Yang, H. Bo, X. Yang, J. Gao, and Z. Shi, "Conditional ls-gan based skylight polarization image restoration and application in meridian localization," in ICASSP 2023 - 2023 IEEE International Conference on Acoustics, Speech and Signal Processing (ICASSP). IEEE, Jun. 2023.

[45] X. Wang, J. Gao, and N. W. Roberts, "Bio-inspired orientation using the polarization pattern in the sky based on artificial neural networks," Optics Express, vol. 27, no. 10, p. 13681, apr 2019.

[46] L. M. Eshelman and J. A. Shaw, "Visualization of all-sky polarization images referenced in the instrument, scattering, and solar principal planes," Optical Engineering, vol. 58, no. 8, p. 082418, 2019.

[47] G. Horvath, B. Bernath, B. Suhai, and A. Barta, “First observation of the fourth neutral polarizationpoint in the atmosphere,” JOSA, 2002.

[48] G. Horváth and D. Varjú, Polarized Light in Animal Vision. Springer Berlin Heidelberg, 2004.

[49] C. Bellver, “Influence of particulate pollution on the positions of neutral points in the sky at seville (spain),” Atmospheric Environment (1967), vol. 21, no. 3, pp. 699–702, 1987.

[50] K. Coulson, Polarization and Intensity of Light in the Atmosphere. A. Deepak Pub., 1988.

[51] W. Jue, H. Pengwei, Q. Jianqiang, and G. Lei, “Confocal ellipse hough transform for polarization compass in the nonideal atmosphere,” IEEE Transactions on Instrumentation and Measurement, vol. 72, pp. 1–8, 2023.

[52] C. Cornet, L.C-Labonnote, and F.Szczap, “Three-dimensional polarized Monte Carlo atmospheric radiative transfer model (3DMCPOL) : 3D effects on polarized visible reflectances of a cirrusc loud,” Journal of Quantitative Spectroscopy and Radiative Transfer, vol. 111, no. 1, pp. 174–186, jan 2010.

[53] G. Li, Y. Zhang, S. Fan, Y. Wang, and F. Yu, “Robust heading measurement based on improved berry model for bionic polarization navigation,” IEEE Transactions on Instrumentation and Measurement, pp. 1–1, 2022.

[54] S. Vandendriessche, “Polarizer Selection Guide,” https://www.edmundoptics.com/knowledge-center/application-notes/optics/polarizer-selection-guide, (accessed: 20.07.2023).

[55] P. Kovesi, “Good colour maps: How to design them,” arXiv preprint arXiv:1509.03700, 2015.

[56] I. Reda and A. Andreas, “Solar position algorithm for solar radiation applications,” Solar Energy, vol. 76, no. 5, pp. 577–589, 2004.

[57] H. B. Mitchell, Image Similarity Measures. Berlin, Heidelberg: Springer Berlin Heidelberg, 2010, pp. 167–185.

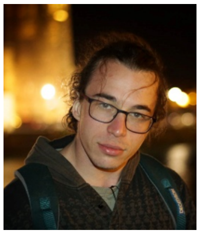

Antoine Moutenet was born in Lyon, France, in 1996. He graduated from the Institut d’Optique Graduate School and also obtained a Master’s degree in Advanced Imaging and Materials Appearance from the Université Jean Monnet in 2020. During his engineering studies he had two 6-month interships, a first in Imagine Optics on low-cost adaptive optics for telescopes and a second in Gaggione SAS on the design of a production control bench for plastic injection molding optics, where he continued as engineer for a few months. He is currently a Safran Electronics & Defense doctoral student at the Institut des Sciences du Mouvement in Marseille, France, where he is developing portable heading sensors. His current research interests include polarimetry and celestial compass navigation.

Léo Poughon was born in Toulouse, France, in 1997. He graduated from Institut d’Optique Graduate School in 2019 in the field of Optical Design while apprenticing at Horiba France where he worked on the development of Spectro-polarimeters in various bands (NIR, Visible, UV). He was the leader of the Institut d’Optique robotics club for three years where he gained experience on rapid prototyping and robotics. He is currently a Ph.D student at the Institute of Movement Sciences in Marseille, France, working on celestial polarization navigation with Stellantis where he developed low-cost heading sensors for vehicles. His current research interests include polarimetry, celestial compass navigation, deep learning, and unconventional imaging.

Bruno Toulon was born in 1984 in France. He graduated from Institut d’Optique Graduate School, France, in 2006 with a specialty in optics and photonics. He worked at Onera, The French Aerospace Lab, on optical measurements of segmented wave fronts by interferometry techniques. He received a Ph.D from the University Paris-Sud in 2009 with his dissertation on Complex Amplitudes measurement by multi-lateral shearing interferometers. He then joined Safran Electronics & Defense, first as optronics engineer for new products and then as Chief Engineer for a defense product in charged of the development team.

Julien R. Serres was born in Aix-en-Provence, France, in 1978. He obtained an Agrégation in Applied Physics (a high-level competitive examination for recruiting teachers in France) at the École Normale Supérieure, Cachan, France, in 2002. He agained his Master’s degree in Medical Imaging from Paris XI University (Now Paris-Saclay University) and a Master’s degree in Electronics, Electrotechnics, and Automatic Control Engineering from Paris XI University and the École Normale Supérieure de Cachan (Now ENS Paris-Saclay), France, in 2003. Later that year, he joined the Biorobotics Lab at the Movement and Perception Institute, C.N.R.S. and Aix Marseille University, Marseille, France, as a Ph.D. student under the supervision of Dr. Nicolas Franceschini. He obtained his Ph.D. at the University of Montpellier II, France, in July 2008. He has been a senior lecturer at Aix Marseille University since 2014 and is a member of the bio-inspired systems team at the Institute of Movement Sciences - Étienne-Jules Marey, France. He is the author of more than 100 publications, including articles published in 29 indexed peer-reviewed journals, and recipient of several best paper awards and honors (IEEE ECMR conference in 2017, Living Machines conference in 2018, The National Trophy IoT Industry & Services in 2019, The 7th International Bionic Award 2020, The 5th County Prize for Research in Provence in 2021). He is a senior member of the Institut Universitaire de France (IUF) from 2022 to 2027. His research interests include bio-inspired robotics and bio-inspired visual localization techniques.

Stéphane Viollet is a research director at the National Center for Scientific Research (CNRS) and currently runs the Bio-inspired Systems team at the Institute of Movement Sciences, Aix Marseille University, France. His research interests include biorobotics, origami-based robotics, sensorimotor control as well as the development of innovative bioinspired visual sensors and control laws for implementing autonomous robots. He received his M.Sc. degree in control engineering from the University of Bordeaux 1 and the Ph.D. degree from the National Polytechnic Institute, Grenoble, France in 2001.

APPENDICES

TABLE III
PARAMETERS FOR SIMULATION OF THE MEASUREMENT AT LAT 43.2337929°N, LONG 5.4441861°E, OCTOBER 20, 2022 AT 03:30PM (LOCAL HOUR, TIMEZONE +2H)

Sensor parameters 1	
pixel size (μm)	3.45
sensor dimensions (pixels)	rows: 2048, columns: 2448
Parameters of the optics	
focal length (mm)	8
conjugation model	r0
misalignment (pixels)	rows: 0, columns: 0
Sun parameters	
sun azimuth (°)	-216.407 (sun from north) + 61.069 (north from camera x axis)
sun elevation (°)	27.3323 (ephemeris computation) for the standard simulation, 0 for Berry model computation for simulation with symmetry breaking
DoLP	
$DoLP_{max}$ (no unit)	0.3
Neutral points parameters	
δ (°)	20 for the standard simulation, 150 for the simulation with symmetry breaking
Luminance/radiance parameters	
Sky number	4
Micro-polarizers parameters	
Maximum angle error (°)	1
Polarization efficiency ε	0.99
Sensor parameters 2	
Number of bits	12
Saturation ratio	1.6 (unsaturated camera)
Signal-to-Noise-Ratio	50

TABLE IV
PARAMETERS FOR SIMULATION OF THE MEASUREMENT AT LAT 43.2337929°N, LONG 5.4441861°E, JANUARY 25, 2023 AT 11H33 (LOCAL HOUR, TIMEZONE +1H)

Sensor parameters 1	
pixel size (μm)	3.45
sensor dimensions (pixels)	rows: 2048, columns: 2448
Parameters of the optics	
focal length (mm)	8
conjugation model	r0
misalignment (pixels)	rows: 0, columns: 0
Sun parameters	
sun azimuth (°)	-159.587 (sun from north) + 358.685 (north from camera x axis)
sun elevation (°)	25.2978 (ephemeris computation)
DoLP	
$DoLP_{max}$ (no unit)	0.7
Neutral points parameters	
δ (°)	0
Luminance/radiance parameters	
Sky number	10
Micro-polarizers parameters	
Maximum angle error (°)	1
Polarization efficiency ε	0.99
Sensor parameters 2	
Number of bits	12
Saturation ratio	0.45 (saturated camera)
Signal-to-Noise-Ratio	50

TABLE V
PARAMETERS FOR SIMULATION OF THE MEASUREMENT AT LAT 43.2869904°N, LONG 5.4033614°E, JULY 12, 2022 AT 10:30AM (LOCAL HOUR, TIMEZONE +2H)

Sensor parameters 1	
pixel size (μm)	3.45
sensor dimensions (pixels)	rows: 2048, columns: 2448
Parameters of the optics	
focal length (mm)	1.8
conjugation model	r2
misalignment (pixels)	rows: 0, columns: 0
Sun parameters	
sun azimuth (°)	-102.224 (sun from north) -225.2610 (north from camera x axis)
sun elevation (°)	44.8146 (ephemeris computation) -5 (manual correction only for Berry model computation)
DoLP	
$DoLP_{max}$ (no unit)	0.5
Neutral points parameters	
δ (°)	10
Luminance/radiance parameters	
Sky number	15
Micro-polarizers parameters	
Maximum angle error (°)	1
Polarization efficiency ε	0.99
Sensor parameters 2	
Number of bits	12
Saturation ratio	0.55 (saturated camera)
Signal-to-Noise-Ratio	50

TABLE VI
PARAMETERS FOR SIMULATION OF THE MEASUREMENT AT LAT 43.2869904°N, LONG 5.4033614°E, AUGUST 26, 2022 AT 08:30PM (LOCAL HOUR, TIMEZONE +2H)

Sensor parameters 1	
pixel size (μm)	3.45
sensor dimensions (pixels)	rows: 2048, columns: 2448
Parameters of the optics	
focal length (mm)	1.8
conjugation model	r2
misalignment (pixels)	rows: 0, columns: 0
Sun parameters	
sun azimuth (°)	-286.046 (sun from north) -225.2610 (north from camera x axis)
sun elevation (°)	-1.2426 (ephemeris computation) +5 (manual correction only for Berry model computation)
DoLP	
$DoLP_{max}$ (no unit)	0.8
Neutral points parameters	
δ (°)	55
Luminance/radiance parameters	
Sky number	13
Micro-polarizers parameters	
Maximum angle error (°)	1
Polarization efficiency ε	0.99
Sensor parameters 2	
Number of bits	12
Saturation ratio	0.9 (saturated camera)
Signal-to-Noise-Ratio	20